Accepted Manuscript

Structural and Magnetic Studies of $Mg_{(1-x)}Zn_xFe_2O_4$ Nanoparticles Prepared by a Solution Combustion Method

C. Choodamani, G.P. Nagabhushana, S. Ashoka, B. Daruka Prasad, B. Rudraswamy, G.T. Chandrappa

PII: S0925-8388(13)01073-6
DOI: http://dx.doi.org/10.1016/j.jallcom.2013.04.152
Reference: JALCOM 28446

To appear in:

Received Date: 11 February 2013
Revised Date: 22 April 2013
Accepted Date: 23 April 2013

Please cite this article as: C. Choodamani, G.P. Nagabhushana, S. Ashoka, B. Daruka Prasad, B. Rudraswamy, G.T. Chandrappa, Structural and Magnetic Studies of $Mg_{(1-x)}Zn_xFe_2O_4$ Nanoparticles Prepared by a Solution Combustion Method, (2013), doi: http://dx.doi.org/10.1016/j.jallcom.2013.04.152

Structural and Magnetic Studies of $Mg_{(1-x)}Zn_xFe_2O_4$ Nanoparticles Prepared by a Solution Combustion Method

C.Choodamani[1], G.P. Nagabhushana[2] , S.Ashoka[3] , B. Daruka Prasad[4], B. Rudraswamy[1†], and G.T.Chandrappa[2†]

[1]Department of Physics, Jnanabharathi campus, Bangalore University, Bangalore - 560 056, India.
[2]Department of Chemistry, Central College Campus, Bangalore University, Bangalore - 560 001, India.
[3] Department of Chemistry,Warsaw university of Technology,Warsaw, 00-662 ,Poland.
[4]Department of Physics, Jawaharlal Nehru Technological University, Ananthapur-515002, India.

Abstract

Nanocrystalline $Mg_{(1-x)}Zn_xFe_2O_4$ (x = 0.0, 0.25, 0.5, 0.75 and 1) ferrites were prepared by a solution combustion method using a mixture of fuels. The structural and magnetic properties of the as-prepared samples were studied using powder X-ray diffraction (PXRD), Fourier transform infrared (FTIR) spectoscopy, scanning electron microscopy (SEM), transmission electron microscopy (TEM), UV-Vis absorption spectra and vibrating sample magnetometer (VSM) measurements. The PXRD analysis of all the samples revealed the single phase cubic structure with the space group $Fd\bar{3}m$. The average crystallite size determined from the PXRD data was found to increase from 12 nm to 25 nm with an increase in the Zn content from x = 0 to x = 1. The IR absorption spectra exhibited two prominent peaks, which are assigned to tetrahedral and octahedral vibrations. The saturation magnetization, magnetic moment and remenant magnetization increases with an increase in the zinc content up to $x = 0.5$ and decrease thereafter. The observed behavior is consistent with Yaffet-Kittel magnetic ordering. The ZFC (zero field cooled) and FC (field cooled) measurements of magnetization revealed that the blocking temperature is well below room temperature.

Keywords: Ceramics, Chemical synthesis, Magnetisation, X-ray diffraction.

[†]Corresponding authors:

Email: brudraswamy@gmail.com, gtchandrappa@yahoo.co.in;

Tel: +91 80 22961489; Department of Physics, Bangalore University, Bangalore-560056, India

Tel: +91 80 22961350; Department of Chemistry, Bangalore University, Bangalore-560001, India.

1. Introduction

Ferrites in nanoscale form are technologically essential materials because of their size dependent electrical, magnetic, mechanical, optical and chemical properties. Mg-Zn ferrite (MZF) is a soft, spinel structured, n-type semiconducting magnetic material. MZF is used in microwave devices, electromagnetic wave absorbers in the VHF/UHF region, high density magnetic recording, magnetic refrigeration, bio-processing and magneto- optical devices because of its high resistivity, high magnetic permeability and low magnetic losses [1-3]. These properties depend on the nature of the ions and their distribution among the tetrahedral (A) and octahedral (B) sites. In the structure of $Mg_{(1-x)}Zn_xFe_2O_4$, one-eighth of the A sites are filled by the divalent cations (Mg^{2+}/Zn^{2+}) and one-half of the B sites are with trivalent cations (Fe^{3+}). The structural and magnetic properties of spinel ferrites can be tuned by selecting the composition and a suitable method of preparation [4]. There are various methods to synthesize ferrites in nanoscale form e.g., co-precipitation [5], solution combustion [6], high energy ball milling [7] and the carboxylic complex precursor method [8]. Recently, the solution combustion method has attracted much attention because, stoichiometrically pure, small-size ferrite particles are formed at low temperatures and in a short amount of time. The solution combustion method is one of the most promising procedure for the large scale production of nanoparticles

The present work is focused on the effect of the zinc content on the structural, morphological and magnetic properties of nano-MZF prepared by the solution combustion method.

2. Experimental

Analytical grade Mg $(NO_3)_2$.$6H_2O$, Zn $(NO_3)_2$.$6H_2O$ and Fe $(NO_3)_3$.$9H_2O$ from Merck Ltd., each with a purity of 99.98%, were used without further purification. In a pyrex dish with a capacity of 300 ml, stoichiometric quantities of the metal nitrates were dissolved in 10 ml of distilled water, to which a mixture of sugar and urea was added as a fuel. The homogeneous mixture in the pyrex dish was rapidly heated in a muffle furnace maintained at 400±10°C. The reaction mixture boils and undergoes thermal dehydration, followed by smoldering with the liberation of gaseous products, such as oxides of nitrogen and carbon to produce foamy, voluminous fine nano-MZF.

For the as-prepared samples, the crystallographic phase analysis has been recorded at room temperature using the PXRD technique. The PXRD measurements were performed using Bruker Axs D8 Advance appratus utilizing monochromatic Cu-Kα radiation wavelength (λ = 1.5406 Å) and scanning the diffraction angle over the range of $20^\circ < 2\theta < 80^\circ$ with a scanning speed of 0.02° min^{-1}. The average crystallite size (D) and lattice constant (*a*) were calculated using the standard relations. The FTIR spectra of the samples dispersed in KBr pellets were recorded on a Fourier transform infrared Nicolet spectrometer over the spectral range from 250 to 4000 cm^{-1}. The surface morphology of the samples was examined using a JEOL JSM-6390LV SEM. The particle size and shape were observed by a JEOL JEM 2100 TEM. The UV-Vis absorption spectra of the samples were recorded on a Varian Cary 5000 Spectrometer in the spectral range of 200 to 2000 cm^{-1}. The magnetization measurements were performed using a Lakeshore 7410 VSM.

3. Results and discussion

3.1 Structural properties

The PXRD pattern for MZF exhibits the crystalline cubic spinel structure of the Fd3̄m (227) space group. A close examination of the PXRD pattern indicates slight variation in the parameters such as peak intensities, peak positions and peak width, with the increase in the zinc content, as shown in Fig.1. The pattern can be indexed to the JCPDS card No. 00-008-0234 [9]. There were no additional peaks corresponding to any intermediate phase. The average crystallite size was calculated using the Debye Scherrer formula $D = (k\lambda/\beta \cos\theta)$, where *D* is the average crystallite size derived from the (311), (220), (400), (511) and (440) peaks of the *PXRD* pattern, k is the sphere shape factor (k=0.9), θ is the Bragg's angle, β is the full width at half maxima of the peaks and λ is the wavelength of x-rays used. The structural parameters, such as average crystallite size (D) and lattice parameter (a) vary with the zinc content in the MZF and are tabulated in Table 1. The average crystallite sizes of all of the synthesized samples were observed to be in the range of 12-25 nm.

The lattice parameter for each peak was calculated using the standard relationship

$$a = \frac{\lambda}{2}\left\{\frac{\sqrt{(h^2+k^2+l^2)}}{\sin(\theta)}\right\} \quad \ldots\ldots\ldots\ldots\ldots \quad (1)$$

where h, k and l are the Miller indices of the relevant crystal plane. The calculated lattice parameter is observed to be in the range of 8.38 Å to 8.44 Å. The variation in the lattice parameter is attributed to the substitution of the smaller Fe^{3+} (ionic radius of 0.67 Å) ions with larger Zn^{2+} (ionic radius of 0.82 Å) ions at tetrahedral sites and the replacement of the Mg^{2+} ions

(ionic radius of 0.66 Å) with the larger radius Fe^{3+} ions at the octahedral sites [10]. For a high concentration of zinc (e.g., x = 1) a decrease in the lattice parameter is observed, which may be attributed to the shifting of some of the Fe^{3+} ions from site A to site B [5].

3.2 FTIR absorption studies

The FTIR spectra for MZF are shown in Fig.2. The absorption peaks at 500-600 cm^{-1} correspond to the intrinsic stretching vibrations of the metal at the tetrahedral site, $M_{tetra} \leftrightarrow O$ whereas the peaks for the octahedral-metal stretching vibration $M_{octa} \leftrightarrow O$ appear in the spectral range of 400-385 cm^{-1}. These bands are characteristics of the spinel structure [11]. The variation of the band positions 'ν_1' and 'ν_2' as a function of the Zn content is tabulated in Table 1. The shift of 'ν_1' and 'ν_2' towards lower frequencies with increasing zinc content may be ascribed to the variation in the lattice constant. The increase in the lattice constant affects the Fe^{3+}– O^{2-} stretching vibrations and is a major cause for change in band positions [12]. In the present study the absorption band ν_1 does not exhibit any splitting, consequently the possibility of Fe^{2+} ions being located at the A-sites is ruled out [13,14]. The splitting in the absorption band at approximately 400 cm^{-1} suggests the occupancy of B sites by Mg^{2+} ions [15]. The absorption band at approximately 3450 cm^{-1} indicates the presence of adsorbed water on the surface of the ferrite nanocrystals [16]. The band at approximately 2350 cm^{-1} is attributed to the presence of small traces of the carbonyl group [17].

3.3 SEM and EDX analysis

The *SEM* micrographs in Figs.3 a and b shows the agglomerated, fluffy and porous nature of the $MgFe_2O_4$ and $Mg_{0.5}Zn_{0.5}Fe_2O_4$ samples respectively. The observed voids and porous regions in the samples are attributed to the release of a large amount of gas during the combustion process. The presence of the porous network is one of the characteristics of combustion synthesized powders [18]. The EDX spectra in Figs.3 c and d show both the composition and the elemental percentage of the above samples. The intensity of the Mg peak in Fig.3d is significantly lower than that of Fig.3c, which reveals that the Zn is substituted for Mg. The EDX of $MgFe_2O_4$ and $Mg_{0.5}Zn_{0.5}Fe_2O_4$ indicate the presence of Fe, Mg, Zn and O as major elements with expected ratio indicates the absence of any impurities

3.4 TEM analysis

The TEM images of samples (Figs. 4 a and b) with composition x = 0.0 and 0.5 were converted into binary form and the particle sizes were analyzed using ImageJ1.46r software. The values of average particle size obtained are about 12 nm and 19 nm respectively for x = 0.0 and 0.5. Hence the sizes obtained from TEM images are consistent with the average crystallite size calculated from Scherrer formula using the PXRD data. The selected area electron diffraction (SAED) patterns of the spotty rings shown in the inset of Figs 4 a and b reveals the polycrystalline nature of the samples. In addition, the bright and sharp rings in the diffraction pattern of both of the samples indicate that the synthesized samples exhibit a high degree of crystallinity. Fig.4b demonstrates that $Mg_{0.5}Zn_{0.5}Fe_2O_4$ powders exhibit a relatively uniform particle distribution.

3.5 Optical band gap studies

The optical band gaps (E_g) of the MZF particles were calculated using Tauc plots of the *UV-Vis* absorption spectra shown in Fig 5 and using the following relationship

$$(\alpha . h\nu) \sim (h\nu - E_g)^n \quad \text{..... (2)}$$

where hν is the photon energy, α is the optical absorption coefficient and n is a constant associated with the different types of electronic transitions. Because oxides are characterized by indirect allowed electronic transitions, the value of n becomes 2 [19]. Extrapolating the linear portion of the curve to $(\alpha h\nu)^2=0$ determines the optical band gap energy. The optical band gap energy for the MZF particles is found to be ~ 2.12 eV, where the slight increase with an increase in the Zn content indicates the structural variation in the samples [20].

3.6 Magnetic properties

The hysteresis curves of the MZF particles measured at room temperature and at 78 K over the field range -20 kOe to +20 kOe are shown in Fig.6. The shape of the curves indicates ferromagnetic nature of samples The magnetic properties such as saturation magnetization (M_s), remenant magnetization (M_r), the ratio of remenant magnetization to saturation magnetization (M_r/M_s), coercive force (H_c), magnetic moment per formula unit in Bohr magneton (n_B) and Yafet-Kittel angles ($\alpha_{y\text{-}k}$) at both temperatures are reported in Table 2. The magnetic moment n_B is calculated from the hysteresis data using the following relationship [21]

$$n_B = (M_w/5525)M_s \quad \text{..... (3)}$$

where 'M_w' is the molecular weight of the ferrite sample and 'M_s' is the saturation

magnetization. On the basis of the spin-only moments of Neel's two-sub lattice model, the Y-K angles are calculated using the relationship

$$\cos\alpha_{YK} = \frac{n_B + B(1-x)}{B(1+x)} \quad \text{.....(4)}$$

The variation of M_s and n_B with increasing Zn^{2+} content is shown in Fig.7. The saturation magnetization and magnetic moment were found to increase with an increase in the Zn^{2+} content up to $x = 0.5$ and then decreases with a further increase of the Zn^{2+} content. The initial increase in the magnetization and magnetic moment can be explained on the basis of the Neel's two sub lattice model. According to Neel three types of exchange interactions exist between the unpaired electrons of the two ions present at the A and B sites i.e., A-A, A-B and B-B. Of these three interactions, the A-B interaction is effective and strong and it oppositely aligns the magnetic spins of the A and B site, therefore the magnetic moment per formula unit (M) of the lattice is

the difference between the moments of the *B* and *A* sub lattices, i.e., $M = |M_B - M_A|$. In MZF both

Mg^{2+} and Zn^{2+} are diamagnetic and according to the site preference Zn ions occupy the A-sites. The addition of the Zn forces the same number of Fe^{3+} ions from A- sites to occupy *B*-sites, as a result the magnetic moment of B-sites increases and hence M_s and n_B increase with increasing Zn^{2+} content. However the decrease in M_s and n_B for $x > 0.5$ indicates the existence of a non-collinear spin canting structure in the system. The presence of the canted spin gives rise to a Y-K angle which compares the strength of the A-B and B-B interactions [22]. An increase in the value of the Y-K angles for the samples with increasing Zn content is attributed to the increased favoring of triangular spin arrangements on *B* sites leading to the reduction in the A-B exchange

interaction and the subsequent decrease in M_s and n_B [23]. Almost all of the Zn^{2+} and Cd^{2+} substituted ferrites exhibit a similar type of canting behavior above a certain limit of their content [24-26]. The magnetic moment per formula unit (M) of $MgFe_2O_4$ and $Mg_{0.5}Zn_{0.5}Fe_2O$ calculated using Neel's two sub lattice model, using cation distribution is 1.35μB and 5.5μB, while the magnetic moment per formula unit from hysteresis data are 0.64 μB and 1.77 μB respectively. Hence the moments calculated using Neel's model is much larger than the values obtained from hysteresis data. These results indicate that the magnetization may not only be linked to dopent concentration. In other words, the observed variation in magnetization can be due to many factors such as cation redistribution, existence of point defects in the spinel structure or the formation of spin glass structure at the nano sizes [27,28]. The small values of M_r/M_s and H_C suggest the existence of multi domain (MD) particles in all the samples [15]. In all the samples, the magnetic parameters at 78 K exhibit higher values than those at 300 K, except for the Y-K angles.

Magnetization measurements under zero-field-cooled (ZFC) and field cooled (*FC*) conditions for the *MZF* particles are shown in Fig.8. The *ZFC* curves are obtained by cooling the sample from room temperature to 20 K without applying an external magnetic field. In the case of FC conditions, after the temperature of the samples reach 20 K, a 500 Oe magnetic field was applied and the magnetization was recorded as the temperature was increased from 20K to 300K. The magnetization in the FC decreases gradually with an increase in the temperature. In ZFC the magnetization increases with an increase in the temperature and each of the ZFC curves exhibits a broad cusp and achieves a maximum at the blocking temperature T_B. The width of the cusp in the ZFC curve indicates the existence of particles with different sizes [29]. The broad peaks observed in our samples indicate a wide distribution of particle sizes, which is confirmed by the TEM and PXRD data. The temperature that corresponds to the bifurcation of the FC and ZFC curves (T_{irr}) is observed at a temperature higher than T_B. In an ideal monodispersed system, T_{irr}

and T_B occur at the same temperature and are sensitive to the applied magnetic field as well as the size distribution of the particles. The observed difference in T_{irr} and T_B suggests the existence of spin-spin or cluster-spin type of interactions [30]. However, the exact type of interaction can be established with field dependent ZFC-FC studies or ac susceptibility studies.

4.Conclusions

MZF nanoparticles were successfully synthesized by a low-temperature solution combustion technique. The effect of Zn on the structural and magnetic properties of Mg-Zn ferrite was studied. PXRD and FTIR studies reveal the formation of a single phase cubic spinel structure. The TEM images indicate that the samples are nanocrystalline in nature. The measured optical band gap energy value substantiates the semiconducting property of the material. The saturation magnetization, magnetic moment and Y–K angles vary with increasing zinc content. The small values of M_r/M_s suggest the existence of multi domain particles in all of the samples. The small values of coercivity indicate that the samples are good materials for quick spin-aligning devices.

Acknowledgment

G.T.Chandrappa thank the University Grants Commission for financial support. One of the authors C.Choodamani thank STIC, CUSAT, Cochin for providing *PXRD*, *SEM* facility and SAIF, IIT Madras for VSM facility. C.C also gratefully acknowledges UGC and Commissionarate of collegiate education for awarding her FIP fellowship to carry out this research work.

References

[1] D. Chen, H.Y. Liu, Mater. Lett. 72 (2012) 96-97.

[2] Y.Y.Meng, Z.W.Liu, H.C. Dai, H.Y. Yu, D.C.Zeng, S. Shukla, R.V. Ramanujan, Powder Technol. 299 (2012) 270-275.

[3] J. Hu, G. Shi, Z. Ni, L. Zheng, A. Chen, Phyisca B. 407 (2012) 2205-2210.

[4] A. Verma, T.C. Geol, R.G. Mendiratta, M.I. Alma, Mater. Sci. Eng. B. 60 (1999) 156-162.

[5] S.S. Khot, N.S.Shinde, B.P. Labgaonkar, B.B. Kale, S.S. Watwe, Adv. Appl. Sci. Res.

2 (2011) 460-471.

[6] K. Suresh, K.C. Patil, J.Mater. Sci. Lett. 13 (1994) 1712-1714..

[7] M. Sinha, H. Dutta, S.K. Pradhan, Physica E. 33(2006) 367-369.

[8] G.P. Nagabhushana, S. Ashok, P. Chichaiah, G.T. Chandrappa, Mater. Lett.91(2013) 272-274.

[9] N. Yahya, A.S.M. Nor Aripin, A.A. Aziz, H. Daud, H.M. Zaid, L.P. Pah, N.Maarof, Am. J. Eng. App. Sci.1(2008), 53-56.

[10] K. A. Mohamed, A.D. Al-Rawas, A.M. Gimelseed, A. Sellai, H.M. Widatallah, A.Yousif, M.E. Elzain, M.Shongwe, Physica B. 407 (2012) 795-804.

[11] R.D. Waldron, Phy. Rev. 99 (1955) 1727.

[12] N.Singh, A. Agarwal, S. Sanghi, P.Singh, J. Magn.Magn.Mater. 323 (2011) 486-492.

[13] A.K. Nikumbh, A.V.Nagawade, G.S. Gugale, M.G.Chaskar, P.P. Bakare, J. Mater. Sci. 37 (2002) 637-647.

[14] E. Melagiriyappa, H.S. Jayanna, J.Alloys. Compd. 482 (2009) 147-150.

[15] B.K. Bammannavar, L.R. Naik, R.B. Pujar, B.K. Chougule, Ind. J. Eng. Mater. Sci.14 (2007) 381-385.

[16] Y. Koseoglu, A. Baykal, F. Gozuak, H. Kavas, Polyhedran. 28 (2009) 2887-2892.

[17] N.Kasapoglu, B.Birsoz, A.Baykal, Y. Koseoglu, M.S.Toprak,Cen.Eur.J.Chem.5(2007) 570-580.

[18]G.P. Nagabhushana, G. Nagaraju, G.T.Chandrappa,J. Mater. Chem. A.1(2013)388-394.

[19] X. Liu, F. Zhou, M. Gu, S.Huang, B.Liu, C.Ni, Opt.Mater.31(2008)126-130.

[20] G.P.Joshi, N.S. Saxena, R.Mangal, A.Mishra, T.P.Sharma, Bull.Mater. Sci.26(2003)387-389.

[21] A.B. Gadkari, T.J. Shinde and P.N. Vasambekar, J. Mater. Sci,- Mater. Electron. 21 (2010) 96-103.

[22] Y. Yafet, C. Kittel, Antiferromagnetic arrangements in ferrites, Phy.Rev.87(1952) 290-294.

[23] S.Geller, Phy.Rev.181(1969)980-985.

[24] P.P. Hankare , U.B.Sankpal , R.P.Patil , A.V.Jadhav, , K.M.Garadkar , B.K.Chougule, J. Magn.Magn.Mater.323(2011)389–393

[25] S.S. Bellad, S.C. Watawe, B.K. Chougule, J. Magn. Magn. Mater.195(1999)57-63.

[26] S.S. Bellad, B.K. Chougule, Mater. Res. Bull.33(1996)1165-1173.

[27] Siddhartha Mal, Sudhakar Nori, Suhrit Mula, J. Narayan, J. T. Prater, J. Appl. Phys. 112, 113917 (2012)

[28] N.M. Deraz, J. Anal. Appl. Pyrolysis. 91 (2011) 48–54

[29] A.S´lawska-Waniewska, P.Didukh, J.M.Greneche, P.C.Fannin, J. Magn. Magn. Mater. 227 (2000) 215-216.

[30] R. Desai, V. Davariya, K. Parekh, R.V. Upadhyay, Pramana. 73(2009)765-780.

Table captions

Table .1: Variation of structural parameters with Zn^{2+} content.

Table.2 : Magnetic parameters at 300 K & 78 K.

Figure captions

Figure 1. *PXRD* pattern of $Mg_{1-x}Zn_xFe_2O_4$ (x = 0.0, 0.25, 0.5, 0.75, 1)

Figure 2. *FTIR* spectra of $Mg_{1-x}Zn_xFe_2O_4$ (x = 0.0, 0.25, 0.5, 0.75, 1)

Figure 3. *SEM* image of (a) $MgFe_2O_4$ and (b) $Mg_{0.5}Zn_{0.5}Fe_2O_4$;

EDAX of (c) $MgFe_2O_4$ and (d) $Mg_{0.5}Zn_{0.5}Fe_2O_4$

Figure 4.*TEM* image of (a) $MgFe_2O_4$ with inset *SAED* pattern (b) $Mg_{0.5}Zn_{0.5}Fe_2O_4$ with inset *SAED* pattern

Figure 5. Energy gap of $Mg_{1-x}Zn_xFe_2O_4$ (x=0.0, 0.25, 0.5, 0.75, 1)

Figure 6.Magnetic hysteresis loops of $Mg_{1-x}Zn_xFe_2O_4$ (x = 0.0, 0.25, 0.5, 0.75, 1) at 300K and 78K .

Figure 7. Variation of magnetization (M_s) and magnetic moment (n_B) at 300 K and 78 K with Zn content

Figure 8. *FC* and *ZFC* magnetization curves of $Mg_{1-x}Zn_xFe_2O_4$ in afield of 500 Oe (x = 0.0, 0.25, 0.5, 0.75, 1)

Table-1

Zn^{2+} content x	Crystallite size (D) nm	Lattice Constant (a) Å	*FTIR* absorption bands(cm^{-1})	
			ν_1	ν_2
0.00	12.6	8.417	558	405
0.25	14.51	8.393	557	400
0.50	18.58	8.429	553	389
0.75	21.17	8.443	546	385

1.00	25.29	8.387	541	372

Table-2

Zn^{2+} Content *x*	**Saturation magnetization (*Ms*) emu/gm**		**Remenant magnetization (*Mr*) emu/gm**		***Mr/Ms***		**Coercive force (*Hc*) Oe**		**Magnetic moment n_B (Bohr magneton)**		**Yafet-Kittel angle ($\alpha_{y\text{-}k}$)°**	
	At 300 K	**At 78 K**	**At 300 K**	**At 78 K**	**At 300 K**	**At 78 K**	**At 300 K**	**At 78 K**	**At 300 K**	**At 78 K**	**At 300 K**	**At 78 K**
0.00	18.993	25.941	8.192	12.786	0.431	0.492	396.86	479.76	0.646	0.888	0	0
0.25	22.715	37.585	7.411	14.976	0.326	0.398	357.65	440.34	0.855	1.414	42.5	34.27

0.50	44.834	90.489	16.061	34.854	0.358	0.385	353.09	394.85	1.770	3.573	55.29	35.93
0.75	16.851	56.489	3.529	13.801	0.209	0.244	365.64	353.87	0.696	2.334	77.14	65.81
1.00	8.075	17.227	3.432	5.1591	0.425	0.299	422.36	451.83	0.348	0.743	86.00	85.73

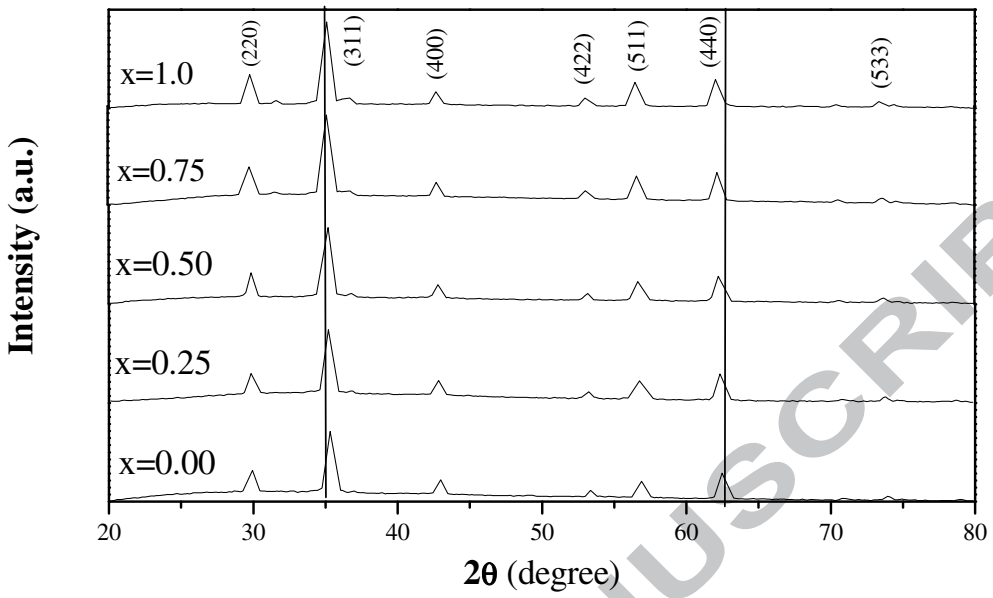

Fig.1

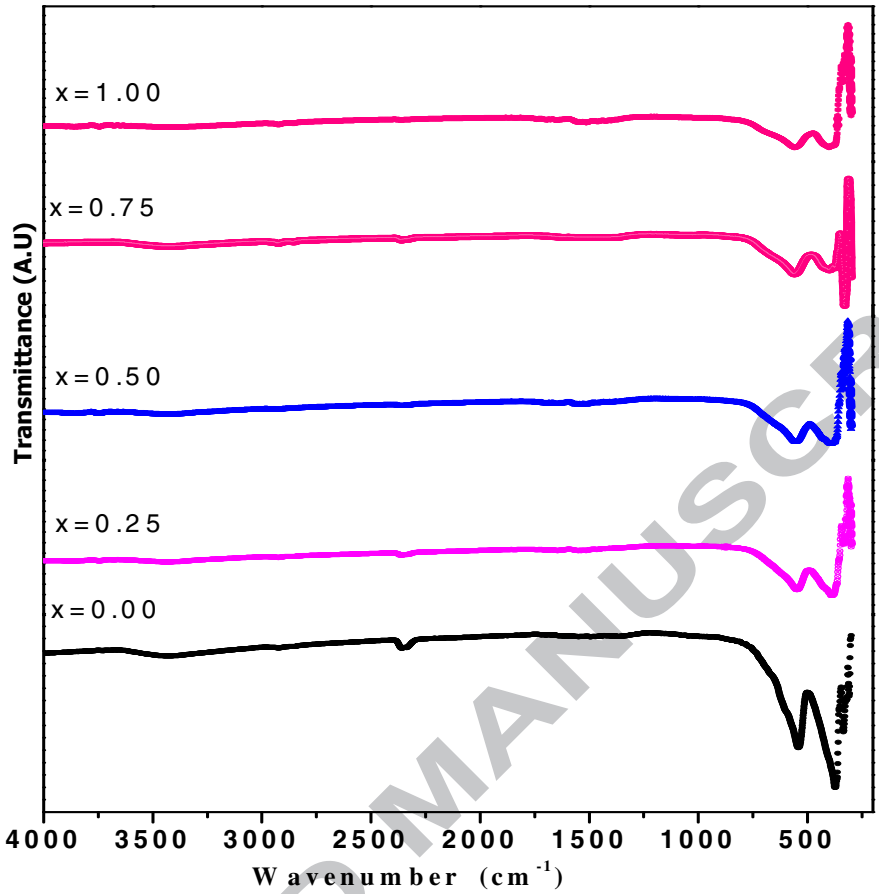

Fig.2

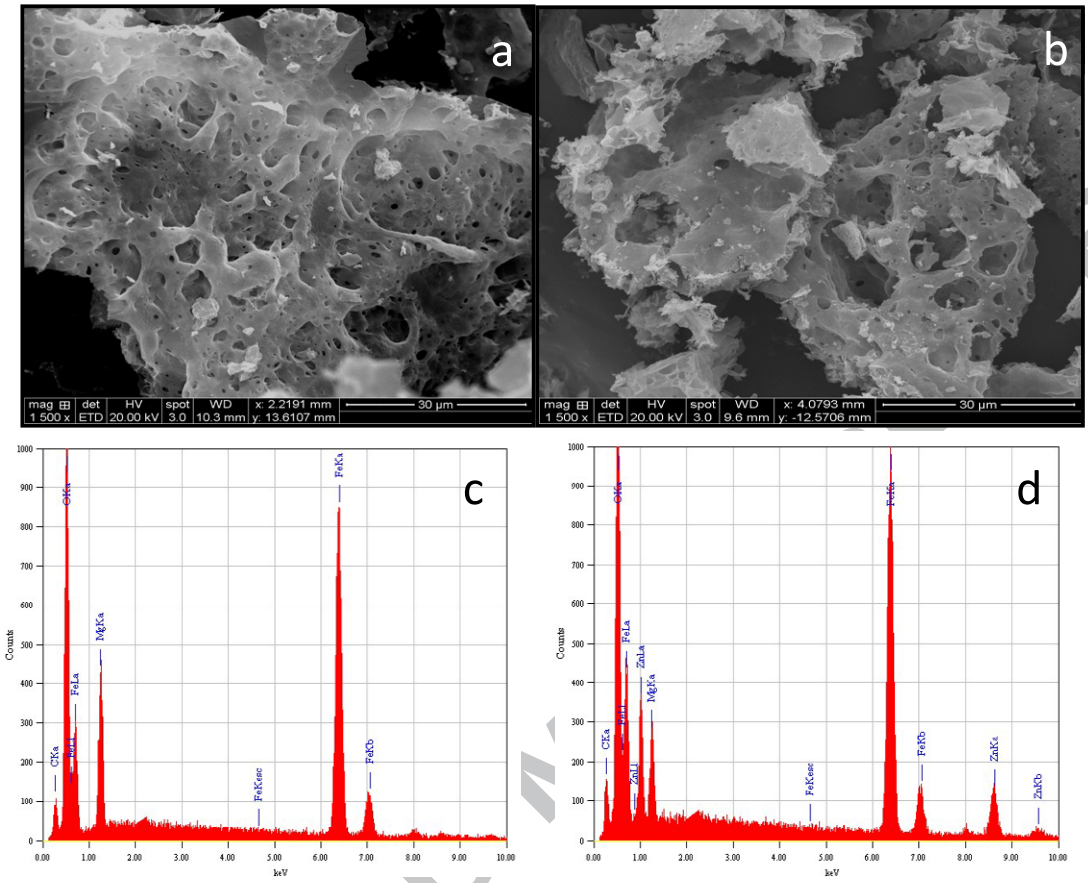

Fig.3

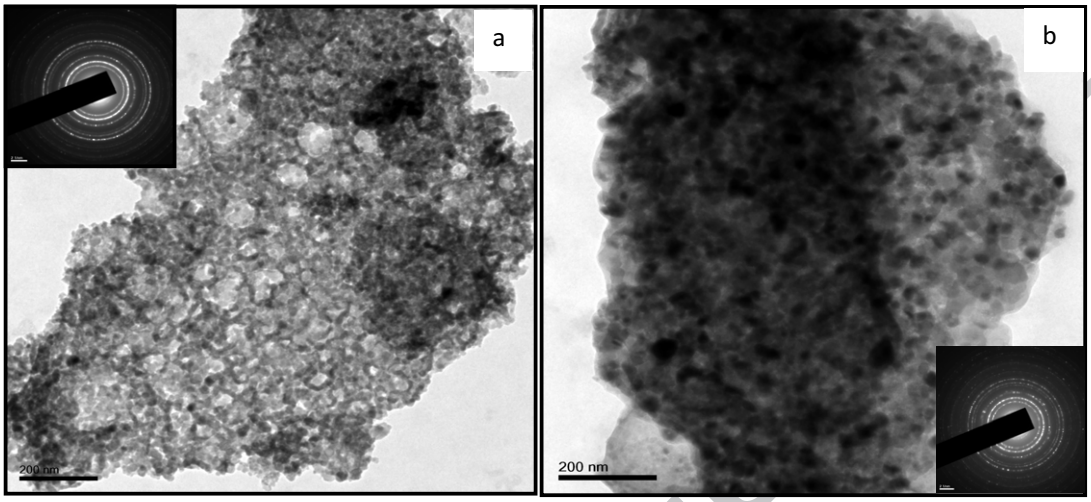

Fig.4

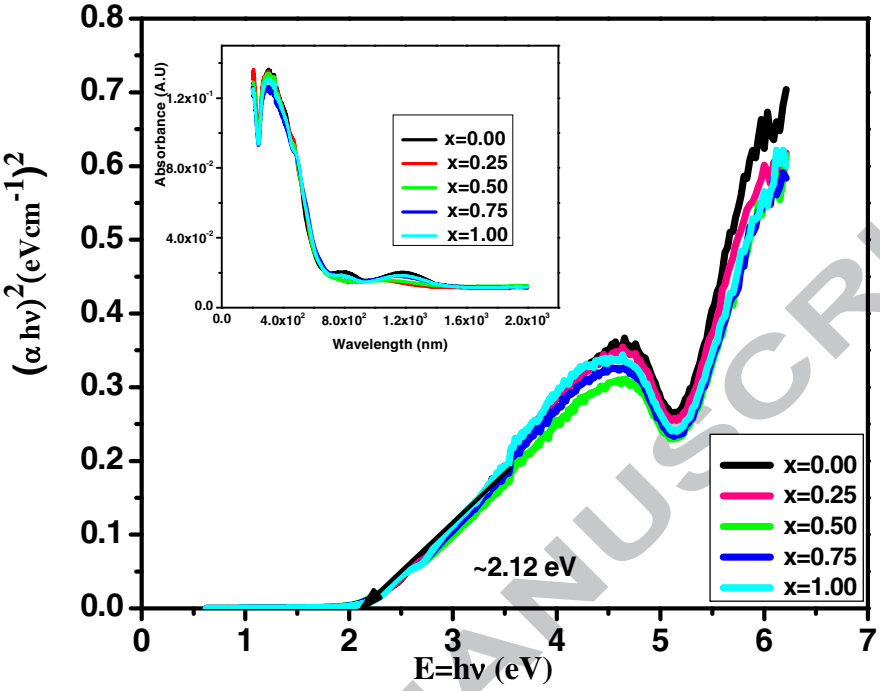

Fig. 5.

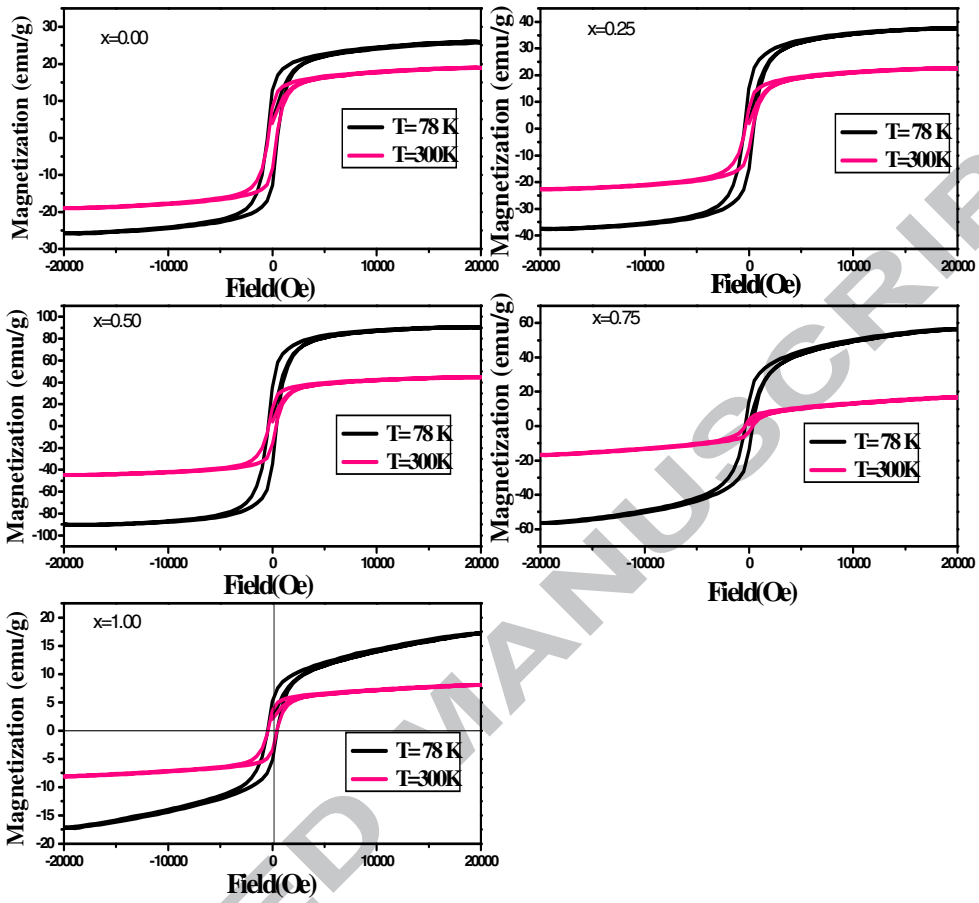

Fig.6

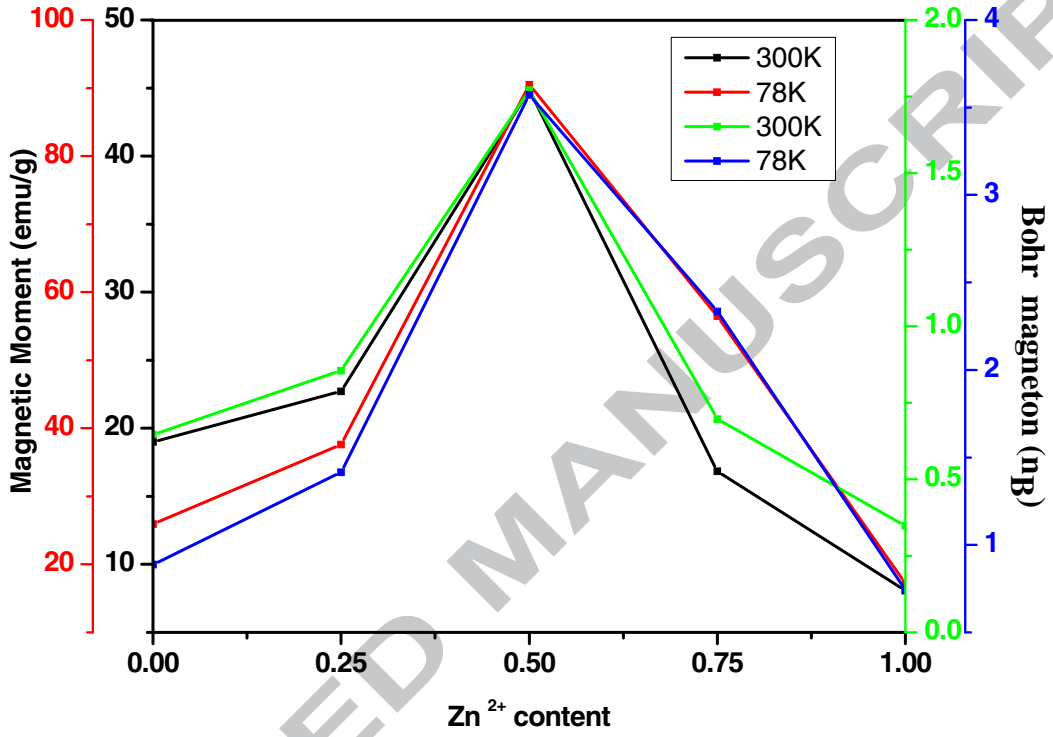

Fig.7

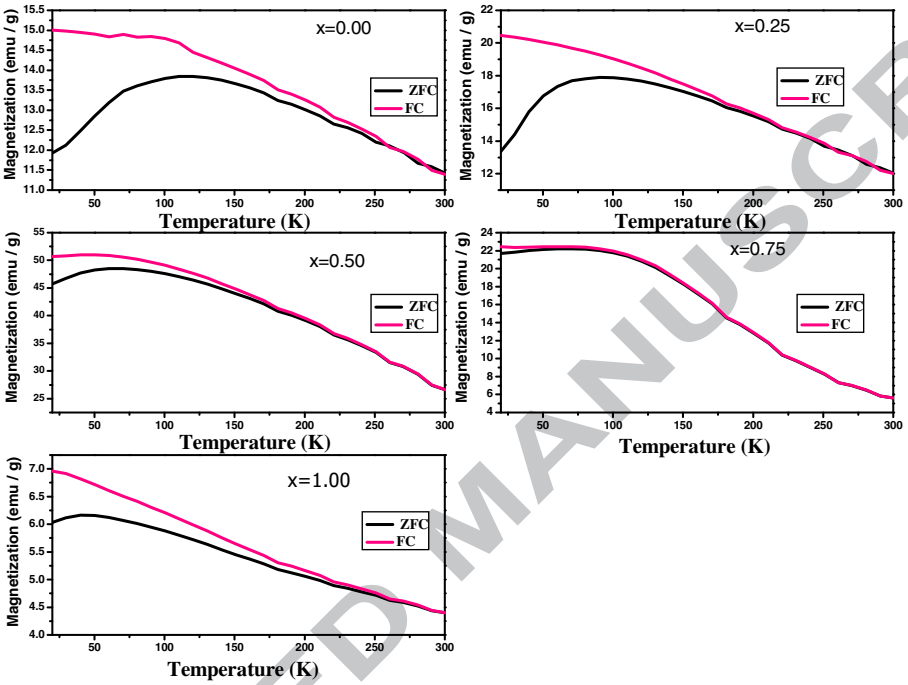

Fig. 8

Highlights

- First time the optimization of combustion synthesis was done with mixture of fuel.
- The characterization of the prepared samples confirms the nanocrystalline nature.
- Magnetic properties of ferrites can be smoothly tuned by the composition.
- The prepared samples are good materials for quick spin aligning devices.